

Polydisperse collision kernels in droplet-laden turbulence with implications for rain formation

Lukas A. Codispoti,* Daniel W. Meyer, and Patrick Jenny

*Institute of Fluid Dynamics, ETH Zürich
Sonneggstrasse 3, 8092 Zürich, Switzerland*

(Dated: October 27, 2025)

The collision kernel of droplets in warm clouds is a crucially important quantity for the parameterization of precipitation in weather and climate models. Nevertheless, its accurate representation remains a challenge, specifically in the bottleneck range $15\ \mu\text{m} < r < 40\ \mu\text{m}$, within which turbulence is believed to be a key contributor to droplet growth. In this work, we address this problem by performing direct numerical simulations of polydisperse inertial particles suspended in three-dimensional turbulence at Reynolds number $Re_\lambda = 418$. Collision statistics are obtained for droplet pairs across the Stokes number range $St \in [0.02, 2]$. Our analysis reveals that polydispersity enhances collisions between light droplets through differential sampling, but attenuates collisions at larger Stokes numbers by rapidly reducing the spatial overlap of droplet clusters. We quantify and discuss this decorrelating effect in bidisperse clustering and compare our DNS results with the model of Onishi & Seifert [*Atmos. Chem. Phys.* **16**, 12441 (2016)]. A novel phenomenological parameterization for the collision kernel is proposed, showing significant improvements in the predictions for the bidisperse case. Finally, we study the broadening of droplet size distributions due to turbulence and demonstrate the influence of fluctuations of the dissipation rate on accelerated droplet growth.

I. INTRODUCTION

Cumulus clouds form in the shallow regions of earth’s atmosphere when moist air ascends and cools, causing water vapor to condense at nucleation sites into small cloud droplets, which then grow and subsequently fall to the ground in the form of rain. How droplets with radii $15\ \mu\text{m} < r < 40\ \mu\text{m}$ can grow to produce precipitation within 30 minutes is an open question in atmospheric physics, since neither condensational growth nor collision-coalescence through gravitational settling are effective in this so-called *bottleneck* range [1]. Increasing evidence suggests that turbulence, the chaotic motion of fluid flow, plays a crucial role in solving this puzzle. The wide range of turbulent scales modifies the spatial distribution of droplets and amplifies relative velocities, so that collision and coalescence is increased compared to quiescent conditions. These enhanced collision rates are quantified through collision kernels—mathematical expressions that describe the rate at which droplets of given sizes encounter and collide. Accurate collision kernel models are essential for cloud microphysics schemes in weather and climate simulations, as they directly control the rate of droplet size distribution (DSD) broadening and the activation of precipitation. However, developing reliable parameterizations remains challenging due to the limited theoretical understanding of droplet–turbulence interactions, scarce in-situ observations, and numerical constraints. Three primary mechanisms are identified by which turbulence enhances droplet collisions: preferential concentration, differential sampling, and the sling effect.

Preferential concentration arises due to the interaction of inertial particles with turbulent vortices, leading to a non-uniform spatial distribution, also referred to as *clustering*. Particles tend to be expelled from regions of large vorticity and accumulate in strain-dominated areas, creating a compressible effective flow of particles [2]. The inertia of a particle is quantified by the Stokes number $St = \tau_p/\tau_\eta$, where τ_p is the particle relaxation time and τ_η is the Kolmogorov time, characterizing the timescale of the dissipative scales. A particle with $St \ll 1$ behaves like a fluid tracer, whereas with $St \gg 1$, particles move ballistically and decorrelate from the carrier flow. In both limits, particles disperse uniformly in space. In between the two extremes and most notably around $St \approx 1$, on the other hand, particles cluster (see, e.g., Refs. [3–5]). Preferential concentration increases the collision rates between inertial particles by increasing the likelihood of particle encounters in regions of high number density.

Polydispersity, the presence of particles with varying sizes, introduces an additional collision-enhancing mechanism. Particles of different sizes interact differently with turbulent structures, leading to decorrelated trajectories and increased relative velocities between them. Also, differently-sized particles tend to cluster in different regions of the domain, meaning that inter-species preferential concentration is reduced. From a phenomenological standpoint, polydispersity merits investigation since cloud droplets are inherently size-distributed in nature. While this mechanism

* lukasco@ethz.ch

has been studied numerically in two-dimensional turbulence (e.g., Ref. [6]) and three-dimensional turbulence at low Reynolds numbers (e.g., Refs. [7, 8]), comprehensive three-dimensional analyses at high Reynolds numbers remain limited due to computational constraints. In the present work, we extend these efforts by conducting a detailed investigation of polydisperse collision dynamics in three-dimensional turbulence at high Reynolds number.

Finally, the sling effect [9] is the mechanism through which particles experience rare extreme turbulent events and are ‘slung’ out of vortices. This phenomenon occurs when particles from different flow regions cross trajectories, creating singularities in phase space, so-called *caustics* [10]. Caustic formation naturally leads to collisions between particles that travel on different branches of the phase-space manifold, i.e., exhibit different velocities while occupying the same location in physical space. The occurrence of caustics implies that inertial particles do not move on a continuum; thus, there is no well-defined Eulerian field that can describe the motion of the particles. The existence of caustics in turbulent suspensions has been confirmed numerically (e.g., [11, 12]) and experimentally [13]. Yet, whether the sling effect is effective for the collision and coalescence of cloud droplets has been the subject of debate in recent years (see, e.g., Refs. [14–16]). Some authors point out that typical cloud droplets exhibit Stokes numbers $\mathcal{O}(St) = 10^{-2} - 10^{-1}$, and are therefore too light to be susceptible to caustic formation. Others have argued that if cloud droplets with larger Stokes numbers exist, these also tend to have large settling parameters, $Sv = \tau_p g / u_\eta$, where g is the gravitational acceleration and u_η is the Kolmogorov velocity. Particles with $Sv > 1$ settle faster under gravity than they interact with the dissipative scales of the turbulent flow, so that inertial clustering and the sling effect are expected to be significantly attenuated. However, measurements in atmospheric clouds are becoming available at ever-increasing resolutions, revealing evidence suggesting that a fraction of droplets in convective clouds experience conditions conducive to inertial clustering and caustic formation, even when average conditions would suggest otherwise [17, 18]. One pathway to create these conditions is via fluctuations of the local turbulent kinetic energy dissipation rate, ε , which arise naturally due to internal turbulent intermittency. Since

$$St = \frac{2r^2 \rho_p}{9\nu\rho_f} \left(\frac{\nu}{\varepsilon}\right)^{-1/2} \propto r^2 \varepsilon^{1/2} \quad (1a)$$

and

$$Sv = \frac{2r^2 \rho_p}{9\nu\rho_f} g (\varepsilon\nu)^{-1/4} \propto r^2 \varepsilon^{-1/4}, \quad (1b)$$

these fluctuations increase the importance of inertial effects while decreasing the influence of gravitational settling. Measurements from high-resolution holographic imaging also indicate that heterogeneous local droplet population and flow conditions are ubiquitous in atmospheric clouds. For example, Thiede et al. [19] report pronounced inertial clustering in warm clouds within parcels on the order of centimeters. Another field study [20] in stratocumulus clouds revealed that local DSDs can be unexpectedly narrow, so that the droplet population averaged over integral scales is not representative of the local conditions. A small fraction of rapidly growing droplets may be enough to ‘seed’ a cloud and create a run-away effect, in which a few droplets grow large enough to trigger rapid subsequent collisions.

In this study, we perform an extensive DNS campaign of fully-resolved, three-dimensional particle-laden turbulence at $Re_\lambda = 418$. Our aim is to elucidate the mechanisms governing droplet collisions in the bottleneck regime of warm-cloud microphysics. In particular, we provide what is, to our knowledge, the most extensive map of the bidisperse collision kernel ever obtained from high-Reynolds-number DNSs, covering droplet pairs within the range $St \in [0.02, 2]$. We compare our results to existing models and propose modifications for the expression of bidisperse clustering as well as a novel parameterization for the bidisperse collision kernel. In addition, we examine the evolution of the DSD and the effect of enhanced local dissipation. This paper is structured as follows: Section II introduces the theoretical framework for the turbulent collision kernel and reviews existing models; Section III details the numerical methodology, including the flow configuration, particle tracking, and collision-detection procedure; Section IV presents the results, beginning with monodisperse collision statistics, and followed by the bidisperse analysis; Section IV C examines DSD broadening in simulations of coalescing droplets; and Section V summarizes the findings, discusses implications for cloud microphysics, and outlines directions for future work.

Before we begin, a few remarks are warranted regarding the influence of the Reynolds number and turbulent intermittency. Atmospheric clouds exhibit Taylor-scale Reynolds numbers of $\mathcal{O}(Re_\lambda) = 10^4$, which is not attainable in DNSs with today’s computing capabilities (fully resolving turbulence at $Re_\lambda = 10^4$ would require $\mathcal{O}(10^2)$ PB of memory). A variational analysis of the impact of the Reynolds number is beyond the scope of this work. Prior work shows Re_λ -insensitivity of clustering for $St \leq 0.2$, modest attenuation for $0.4 \leq St \leq 1$, and enhancement for $St \geq 2$ as turbulent intermittency increases with the Reynolds number [21–23]. Similar trends appear in the collision statistics [24]. The results suggest that Re_λ mainly affects cloud microphysics by reshaping the distribution of the local dissipation (its intermittency), not by altering the small-scale mechanics at fixed St . In other words, the dominant influence of the Reynolds number is statistical through the intermittency of ε rather than dynamical at the

droplet-scale. Our strategy is therefore to use an isotropic homogeneous turbulent flow field at $Re_\lambda = 418$, with small droplets suspended in the fully-resolved dissipative range, and to compute the collision statistics within small control volumes in the order of $\mathcal{O}(10\eta^3)$. The results are mapped across Stokes number pairs to produce portable kernels that can be embedded in large-scale simulations by combination with an externally supplied ε distribution.

II. TURBULENT COLLISION KERNEL

We consider collisions between droplet pairs (i, j) with radii (r_i, r_j) , separated by the distance $\Delta\mathbf{x} = \mathbf{x}_i - \mathbf{x}_j$ with the relative velocity $\Delta\mathbf{v} = \mathbf{v}_i - \mathbf{v}_j$. The number of collisions per unit time is given by the collision rate \mathbb{N}_{ij} , and the dynamic collision kernel

$$\Gamma_{ij} = \mathbb{N}_{ij}/(n_i n_j) \quad (2)$$

is thence obtained by normalizing with the respective number densities, n_i and n_j (in the monodisperse case with $i = j$ the kernel is multiplied by 2). The widely used kinematic formulation [25, 26]

$$\Gamma = 2\pi R^2 \langle w_r \rangle g(R) \quad (3)$$

serves as the basis for most modeling approaches. Here,

$$w_r = \frac{|\Delta\mathbf{v} \cdot \Delta\mathbf{x}|}{|\Delta\mathbf{x}|} \Big|_{|\Delta\mathbf{x}|=R} \quad (4)$$

is the radial relative velocity (RRV) and $g(R)$ is the radial distribution function (RDF) at contact distance $R = r_i + r_j$. The RDF quantifies the degree of preferential concentration. Its bidisperse form is symmetric ($g_{ij}(r) = g_{ji}(r)$) and computes as

$$g_{ij}(r) = \frac{\langle N_j \rangle_i(r)/V_{\text{shell}}}{N_{ij}V}, \quad (5)$$

where $\langle N_j \rangle_i(r)$ is the average number of particles of species j separated from a particle of species i by a distance within the spherical shell volume $V_{\text{shell}} = \frac{4\pi}{3}[(r + s/2)^3 - (r - s/2)^3]$ of thickness s , N_{ij} is the total number of (i, j) particle pairs, and V is the total system volume. Essentially, Eq. (3) states that the combined effects of differential sampling, preferential concentration and the sling effect can be represented by the product $\langle w_r \rangle g(R)$.

Due to the massive separations of length scales of atmospheric flows, precipitation must be parameterized in weather and climate models rather than resolved directly. Large-eddy simulations (LESs) with grid spacing of $\mathcal{O}(10\text{ m})$ have become the tool of choice to numerically investigate cloud droplet growth and develop such parameterizations. In LES frameworks, the collision kernel is of central importance, as it quantifies growth by collision-coalescence. Typically, the kinematic form (Eq. (3)) is adopted, with $\langle w_r \rangle$ and $g(R)$ modeled separately based on droplet properties and local flow conditions. For example, two recent studies [27, 28] have applied this approach in state-of-the-art LES, showing that turbulence markedly broadens the droplet size distribution in convective clouds. Both relied on the celebrated kernel of Ayala et al. [29]. However, the Ayala kernel was developed for droplets with settling parameters $St > 1$, where gravitational effects dominate over turbulent interactions. Since cloud droplets within the bottleneck range tend to exhibit $St < 1$, new developments are needed to accommodate the turbulent collision enhancement across the full range of droplet sizes relevant to warm rain formation.

A. Onishi model for the turbulent collision kernel

We proceed with a discussion of the Onishi model for the turbulent collision kernel, which shall serve as a benchmark for comparison with our DNS results and newly-proposed parameterization later on. Originally proposed by Onishi et al. [22] and later refined by Onishi & Seifert [23], it represents, to the best of our knowledge, the most comprehensive and advanced parameterization of the turbulent collision kernel currently available for non-sedimenting droplets. The model provides an empirically fitted expression for the monodisperse RDF

$$g_{ii}(R) - 1 = \begin{cases} A_1 St^2 & (\text{for } St_i < St_a) \\ A_2 Re_\lambda St^{-2} & (\text{for } St_a \leq St_i), \end{cases} \quad (6)$$

where $A_1 = 110$, $A_2 = 0.38$ and $St_a = ((A_2/A_1)Re_\lambda)^{1/4}$ (the full formulation is given in Section A). The explicit Re_λ -dependence in the model accounts for the attenuation and enhancement of preferential concentration that arise from increased internal intermittency at larger Reynolds numbers. Below the threshold St_a ($= 1.096$ in our case), clustering is not sensitive to Re_λ , and the scaling $g_{ii}(R) - 1 \propto St_i^2$ is recovered, consistent with the leading-order approximation for $St_i \ll 1$ derived by Wang et al. [30].

Observations suggest that particles with different Stokes numbers cluster in different regions of space. For the bidisperse case, the Onishi model employs the Zhou formulation [8], which expresses the bidisperse RDF in terms of the monodisperse value of each species as

$$g_{ij}(R) = 1 + \rho_{ij}[(g_{ii}(R) - 1)(g_{jj}(R) - 1)]^{1/2}, \quad (7)$$

where ρ_{ij} is a correlation coefficient, which quantifies the spatial overlap between the droplet clusters of species i and j . The droplet groups are never anti-correlated, hence $0 \leq \rho_{ij} \leq 1$. If the particles of both species cluster in the same locations of space, $\rho_{ij} \approx 1$, whereas $\rho_{ij} \rightarrow 0$ if the clusters are completely decorrelated. The authors state that the correlation coefficient can to leading order be obtained as a function of St_j/St_i , and that this function is symmetric around one, so that the modelling task reduces to fitting a model $\rho(\phi)$, where $\phi = \max(St_i/St_j, St_j/St_i)$. The two regions $1 \leq \phi \leq 2.5$ and $\phi > 2.5$ were fitted separately to DNS data at $Re_\lambda = 45$ and connected by a tanh smoothing function, resulting in the composite expression

$$\rho_{ij} = 2.6 \exp(-\phi) + 0.205 \exp(-0.0206\phi)^{1/2} [1 + \tanh(\phi - 3)]. \quad (8)$$

Finally, Onishi and co-authors employ the model of Wang et al. [30] to evaluate the RRV. In this framework, $\langle w_r \rangle$ is composed of a shear-induced and an acceleration-induced contribution, $\langle w_r \rangle^2 = \frac{2}{\pi}(w_{\text{shear}}^2 + w_{\text{accel}}^2)$, a separation adopted in many recent models (see Ref. [29] for a review), where differential sampling in polydisperse suspensions contributes primarily through the acceleration term. Explicit expressions for w_{shear} and w_{accel} following Wang et al. [30] are given in Section B.

III. METHODS

Inertial particles suspended in three-dimensional homogeneous isotropic turbulent flows are considered. The flow velocity field $\mathbf{u}(\mathbf{x}, t)$ is the solution of the incompressible Navier-Stokes equations. We neglect gravity, implying that $St \ll 1$. Furthermore, we assume that particles are small ($r \ll \eta$, where η is the Kolmogorov length scale) and heavy compared to the carrier gas ($\rho_p/\rho_f = 800$). Under these conditions, particles neither disturb the flow nor experience significant hydrodynamic interactions, allowing their motion to be described by the point-particle approximation

$$\dot{\mathbf{x}} = \mathbf{v}, \quad \dot{\mathbf{v}} = \frac{\mathbf{u}(\mathbf{x}, t) - \mathbf{v}}{\tau_p}. \quad (9)$$

Here, $\mathbf{x}(t)$ and $\mathbf{v}(\mathbf{x}(t), t)$ are the Lagrangian particle position and velocity, respectively. The point-particle approach is justified for atmospheric clouds, where typical droplet volume fractions $\Phi_p = \frac{1}{V} \sum_{i=0}^{N_p} \frac{4}{3} \pi r_i^3$ are of the order of $\mathcal{O}(\Phi_p) = 10^{-6}$ [1]. Throughout this work, we will use the terms 'particle' and 'droplet' interchangeably.

We utilize flow fields of forced isotropic homogeneous turbulence obtained from the Johns Hopkins Turbulence Database [31]. These fields are generated by solving the incompressible Navier-Stokes equations using a pseudo-spectral method. The computational domain consists of a periodic cube of length $L = 2\pi$, discretized into $N_g = 1024^3$ grid points. The Taylor-scale Reynolds number is $Re_\lambda = 418$, while the Kolmogorov length and time scales are $\eta = 0.0028$ and $\tau_\eta = 0.0424$, respectively. Equation (9) is solved for large ensembles of particles by trilinearly interpolating the flow velocity to the particle positions and using an integration scheme adapted from Jenny et al. [32]. We use an in-house parallel solver designed to run on massively parallel compute architectures. The computational domain is split into slabs along the x -direction, and particles are distributed across mpi [33] ranks. While treated as points, each particle is assigned a mass m , from which the radius $r = (3m/(4\pi\rho_p))^{1/3}$ and relaxation time $\tau_p = 2r^2\rho_p/(9\nu\rho_f)$ follow.

Collision statistics are computed using the ghost-collision approach, where particles pass through each other without interaction. We determine the collision rate by counting the number of pairs per unit time satisfying the contact condition $|\Delta\mathbf{x}| < R$. To count efficiently, a binary tree data structure is constructed on each rank during every time step, and particles close to boundaries are exchanged with the neighboring ranks to check for inter-rank collisions. Spherical shells of thickness $s = 0.1R$ are used to obtain consistent results for the RRV and RDF (see Ref. [30]), and the results are averaged over ensembles of $N = 10^8$ particles. It was verified that the dynamic (2) matches the kinematic collision kernel (3) within statistical uncertainty.

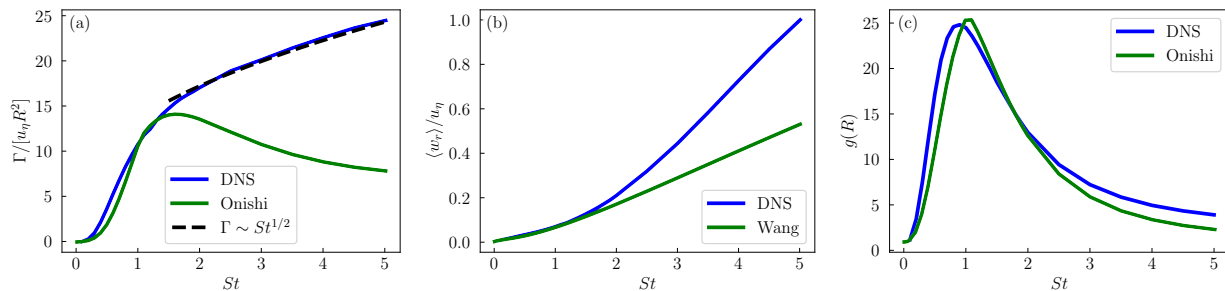


FIG. 1. Monodisperse (a) collision kernel, (b) RRV and (c) RDF at contact as a function of the Stokes number. The blue lines depict the DNS data, whereas the green lines show the results from the model expressions.

We initialize $N_p = 5 \cdot 10^8$ particles per Stokes number uniformly at random in the domain. Precursor simulations are performed for a time $t_0 = 165\tau_\eta$ to ensure statistical stationarity of the collision rate. The simulations are then restarted from t_0 and the ghost collision algorithm is used to detect collisions. When clustering is strong, colliding particles tend to come into contact again later in time. To avoid overestimation of the collision rate in these cases (specifically for monodisperse suspensions), the results collected during the first ten time steps are discarded to exclude repeated contacts between particles that had already collided at times $t < t_0$. Each pair is only allowed to collide once. Particle trajectories are linearly extrapolated to detect in-between-time step collisions.

For the simulations with coalescence, we assume a collision efficiency of one. The number of initialized particles varies between runs, as documented in Table I, as to keep the volume fraction $\Phi_p = 8.5 \cdot 10^{-6}$ constant. Particles that initially overlap with others are removed from the simulation. Each colliding particle pair (i, j) is replaced by a new particle introduced at the position $\mathbf{x}_{\text{new}} = (m_i \mathbf{x}_i + m_j \mathbf{x}_j) / (m_i + m_j)$ with mass $m_{\text{new}} = m_i + m_j$ and velocity $\mathbf{v}_{\text{new}} = (m_i \mathbf{v}_i + m_j \mathbf{v}_j) / (m_i + m_j)$.

IV. RESULTS

A. Monodisperse suspensions

The monodisperse collision statistics are shown in Fig. 1. In panel (a), the collision kernel obtained from the DNS (blue) and from model expressions (green) are plotted versus the Stokes number. The kernels are scaled by $R^2 u_\eta$, the characteristic collision volume swept per unit time by a flow tracer of radius R . The collision kernel increases rapidly with the Stokes number, most notably in the range $0.3 \leq St \leq 1$. At larger St , the collision kernel scales as $\Gamma \sim St^{1/2}$, as shown by the dashed black line. The dependence of the collision kernel on the Stokes number can be understood by examining the two terms appearing in Eq. (3): the RRV and the RDF at contact, shown in Figs. 1(b) and (c), respectively. The growth of $\langle w_r \rangle$ is gentle and approximately linear at first, but increases more rapidly at larger St . This behavior is attributed to the sling effect, which becomes increasingly important and biases the relative velocity statistics between same-sized particles at contact. The RDF, on the other hand, is notably non-monotonic. Particles disperse homogeneously in space with $St \rightarrow 0$ and $St \rightarrow \infty$, respectively, resulting in $g(R) = 1$ in both limits. In between, the RDF peaks at $St \approx 1$, commonly known to be the Stokes number with maximum clustering. The dependence of Γ on the Stokes number can thence be interpreted as the combined effect of $\langle w_r \rangle$ and $g(R)$. It is tempting to attribute the steep increase of the collision kernel between $St \approx 0.3$ and $St \approx 1$ solely to preferential concentration, since the RDF grows at a slope far greater than that of the RRV. However, separating preferential concentration and the sling effect in this manner is not possible, since caustics are also involved in facilitating clustering [34]. In an elegant study, Vosskuhle et al. [35] showed that the sling effect already significantly contributes to the collision dynamics at $St \gtrsim 0.75$, yet the ensemble-averaged RRV only weakly affects the product $\langle w_r \rangle g(R)$ in this range.

While preferential concentration decreases with Stokes numbers exceeding $St = 1$, the RRV continues to grow. Beyond $St \gtrsim 2$, our data suggests a scaling of the collision kernel proportional to $St^{1/2}$. This scaling is consistent with theoretical predictions [36, 37] of the RRV in the sling-dominated regime at high Reynolds numbers, where the motion of the individual particles becomes increasingly uncorrelated with the instantaneous flow field and the motion of other nearby particles. In this regime, particle velocities are randomly distributed, making a gas-kinetic approach following Abrahamson [38] more appropriate. It has been suggested that the collision kernel should be expressed as the sum $\Gamma = \Gamma_{\text{adv}} + \Gamma_{\text{sling}}$, explicitly differentiating between the collision of particles that experience caustics and

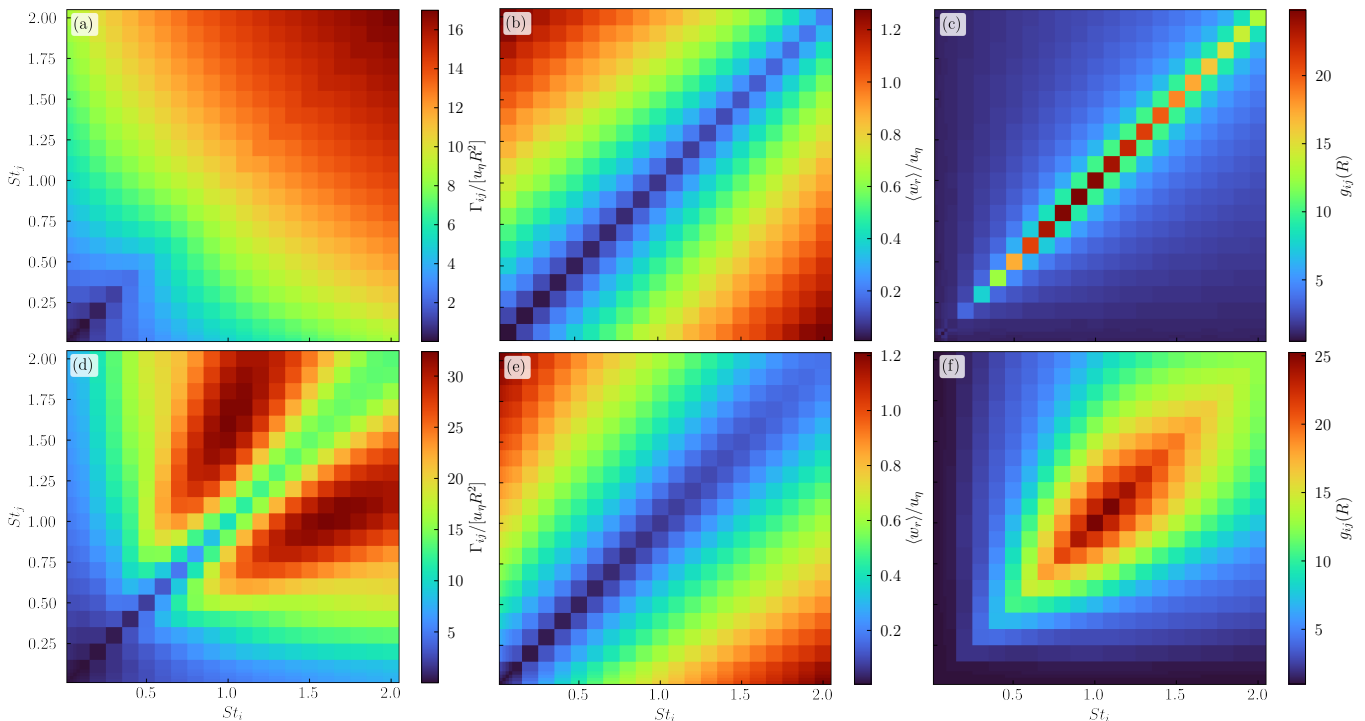


FIG. 2. Bidisperse (a,d) collision kernel, (b,e) RRV and (c,f) RDF at contact obtained from the DNS (top row) and from the Onishi/Wang model (bottom row).

those that do not [35, 36].

The Onishi model provides a remarkably good estimate for the monodisperse RDF, especially considering that the model was used 'out-of-the-box', without re-fitting the parameters to our DNS data. The Wang model, on the other hand, underestimates $\langle w_r \rangle$ for $St \gtrsim 1.5$, i.e., it does not predict well the increased relative motion of heavier particles due to the sling effect. As a result, the Onishi model expression for the monodisperse collision kernel provides results that agree well with the DNS data for Stokes numbers $St \lesssim 1.5$, but fails to reproduce the $\Gamma \sim St^{1/2}$ scaling at larger St .

B. Bidisperse suspensions

Now, how does polydispersity, naturally occurring in cloud droplet populations, affect the collision dynamics? To address this question, we compute the collision kernel, RRV and RDF at contact for droplet pairs (i, j) with Stokes numbers ranging from $St = 0.02$ to $St = 2$. The results are shown in the top row of Fig. 2 as pseudocolor matrices mapped across the Stokes number pairs, while the bottom row shows the corresponding model predictions. The complete map of the collision kernel is provided in Table II for future reference.

It is readily verified that all matrices are symmetric. In agreement with the monodisperse results, the collision rate generally increases with the Stokes number, resulting from the combined effects of $\langle w_r \rangle$ and $g(R)$. We observe that the RRV increases with the separation of the Stokes numbers of the colliding pair, i.e., $\langle w_r \rangle_{ij} \geq \langle w_r \rangle_{ii}$ and $\langle w_r \rangle_{ij} \geq \langle w_r \rangle_{jj}$. The enhancement of the RRV due to differential sampling is largely outweighing its increase along the diagonal. Conversely, the RDF is pronounced along the diagonal and quickly drops as the Stokes numbers separate. This is indicative of the rapid decorrelation of the particle clusters due to differential sampling.

We observe that the behavior of the bidisperse kernel falls into two regimes. At small Stokes numbers (i.e., when both $St_i, St_j \lesssim 0.5$), polydispersity enhances the collisions even if it involves reducing the Stokes number of one of the colliding droplets. This behavior is evident in Fig. 2(a): starting from a point on the diagonal ($St_i, St_j \leq 0.5$), moving horizontally to the left or vertically downward—thus decreasing one Stokes number while keeping the other fixed—results in an increase in Γ . To explain this behavior, consider the competing effects of polydispersity to decrease particle clustering yet increase relative motion. At small Stokes numbers, particles tend not to detach from the flow, and preferential concentration is weak. As a result, the enhancement of the relative velocities due to differential sampling is more significant, and the net effect of polydispersity on the collision kernel is positive. Conversely, at

larger Stokes numbers, $St \gtrsim 0.5$, preferential concentration significantly contributes to the collision rate, and the loss of clustering due to polydispersity outweighs the increased relative velocities, leading to an attenuation of collision. In this regime, the collision kernel increases only when one of the Stokes numbers—and thus the overall inertia of the droplet pair—becomes larger.

James & Ray [6] have reported bidisperse collision kernels obtained from DNS of two-dimensional particle-laden turbulence. Their data show a pronounced increase in the collision rate along the diagonal, indicating that collisions between equal-sized particles are strongly enhanced. Our results do not exhibit this behavior; instead, the collision kernel varies smoothly with the Stokes number separation. In preparing this paper, we identified that this discrepancy may arise from the algorithm used to detect collisions. In monodisperse suspensions, droplets that have collided can remain in contact over prolonged periods of time or re-enter contact later on, leading to an overestimation of the collision rate—most notably under conditions of strong clustering. To mitigate this effect, the first ten time steps of the detection procedure are discarded, and each droplet pair is allowed to collide only once, as described in Section III. More fundamentally, the use of two-dimensional turbulence limits the applicability of their results to atmospheric conditions. The distinct characteristics of 2D turbulence, such as the inverse energy cascade, may not accurately capture the collision dynamics relevant to cloud droplets. Two-dimensional turbulence lacks the flow structures and intermittency associated with three-dimensional turbulence, which are possibly crucial for the collision dynamics of cloud droplets. For example, it has been demonstrated [11, 12] that caustic formation occurs through specific flow topologies unique to 3D turbulence. Moreover, Onishi & Vassilicos [21] compared the collision statistics in 2D and 3D DNS and found that inertial clustering is reduced with increasing Re_λ due to internal intermittency, absent in 2D turbulence.

Figure 2(d) shows the collision kernel obtained from the Onishi model, with the corresponding expressions for $\langle w_r \rangle$ (Wang model, see Section B) and $g_{ij}(R)$ (Eqs. (6) to (8)) shown in Figs. 2(e) and (f), respectively. We find that the Wang model for the RRV provides qualitatively good estimates for the bidisperse case. For $St < 1.0$, $\langle w_r \rangle$ agrees with the DNS results to within 10%. Larger errors are observed mainly for differently-sized particles at larger Stokes numbers, for which the Wang model underestimates the relative velocities due to differential sampling. The bidisperse RDF, on the other hand, is not estimated accurately by the Zhou model. The DNS data displays a much more rapid decorrelation of the droplet clusters compared to the predictions provided by Eq. (8). As a result, the Onishi model strongly overestimates the bidisperse collision kernel, specifically for droplet pairs with Stokes numbers $St_i, St_j > 1$. The relative error with respect to the DNS data of the Onishi model is shown in Fig. 4(c).

1. Bidisperse correlation coefficient

The comparison of Figs. 2(c) and (f) shows that the Zhou model overestimates bidisperse clustering, indicating that the correlation coefficient $\rho(\phi)$ prescribed by Eq. (8) decays too slowly with increasing ϕ . Indeed, we find that the droplet clusters decorrelate much more rapidly than predicted by Eq. (8), as shown in Fig. 3(a), where we plot the correlation coefficient $\rho_{ij} = (g_{ij}(R) - 1)/[(g_{ii}(R) - 1)(g_{jj}(R) - 1)]^{1/2}$ obtained from the DNS and compare it to the Zhou model. The correlation coefficient is shown as a function of St_i/St_j for fixed St_j and varying St_i . We find that the predictions of the Zhou model generally do not agree well with the DNS data. Furthermore, we observe that the behavior of ρ as a function of ϕ does not collapse on a single curve. Instead, we see a multivalued dependence of ρ on ϕ , where the data points with $St_j \lesssim 0.4$ appear to be outliers. Additionally, we find that the correlation coefficient is not symmetric around $St_i/St_j = 1$, such that the simplification used in the derivation of Zhou et al. [8] is not justified.

We now provide arguments to explain the observed behavior. First, we ask why the Zhou model systematically overestimates the bidisperse overlap. Similar discrepancies were reported by Ayala et al. [29], who attributed them to the absence of gravity. As far as we know, there are no prior studies that assess the viability of Eq. (8) for non-sedimenting droplets. We attribute the observed discrepancy to Reynolds number effects not captured in the original Zhou formulation, which was developed at $Re_\lambda = 45$. In contrast, the $Re_\lambda = 418$ flow used in this study exhibits a much wider scale separation. Particles with $St > 1$ tend to cluster within the inertial range of turbulence [12, 39]. At larger Re_λ , the broader range of accessible turbulent scales allows these particles to 'select' increasingly distinct eddy structures, thereby accelerating the loss of correlation between clusters. In contrast, $St < 1$ particles respond mainly to the dissipative scales, explaining why their behavior remains closer to the Zhou prediction. Phenomenologically, ρ must therefore depend on Re_λ , otherwise Eq. (7) overpredicts $g_{ij}(R)$ at large Reynolds numbers. Importantly, the observed discrepancy does arise from the functional form of Eq. (8). We find that at small ϕ , $\rho(\phi) \sim \exp(-\phi)$ provides an excellent approximation, and by re-fitting the parameters appearing in Eq. (8) to our DNS data at $Re_\lambda = 418$, we obtain a curve that agrees much better with the DNS benchmark (black dashed-dotted line in Fig. 3(a)).

Note that the cross-species correlation coefficient is symmetric, i.e., $\rho(St_i, St_j) = \rho(St_j, St_i)$. The apparent asymmetry around $St_i/St_j = 1$ in Fig. 3(a) arises because ρ is plotted as a function of St_i/St_j while St_j is held fixed. For

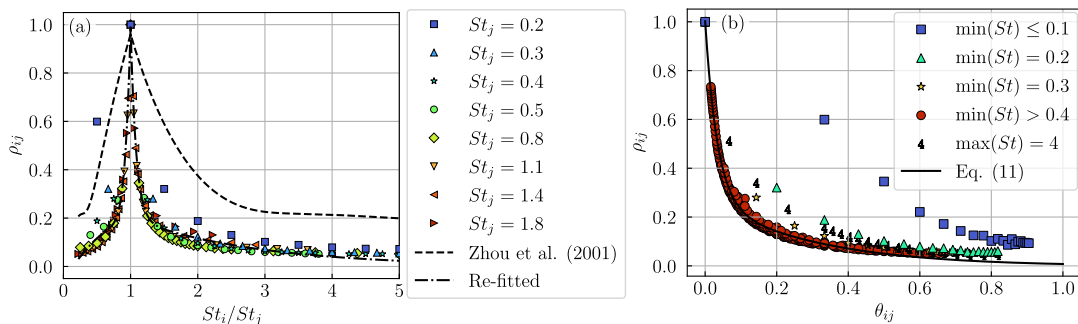


FIG. 3. (a) Bidisperse correlation coefficient as a function of St_i/St_j obtained from the DNS for a range of St_j (colored symbols) and obtained from the Zhou model with the original ($Re_\lambda = 45$, black dashed line) and re-fitted ($Re_\lambda = 418$, black dashed-dotted line) parameters, respectively. (b) Correlation coefficient as a function of θ_{ij} obtained from the DNS (symbols) and the prediction from Eq. (11) (black solid line).

$St_i < 1$, decreasing St_i approaches the tracer limit, leading to a faster decay of the cross-correlation. The asymmetry $\rho(St_i/St_j) \neq \rho(St_j/St_i)$ motivates the use of an alternative parameter to replace $\phi = \max(St_i/St_j, St_j/St_i)$ in modeling the correlation coefficient. The dispersion parameter

$$\theta_{ij} = \frac{St_i - St_j}{St_i + St_j} \quad (10)$$

provides a suitable alternative, as the collision statistics are naturally symmetric with $\theta_{ij} = -\theta_{ji}$, so that the modeling task reduces to finding an expression for $\rho(\theta)$, where $\theta = |\theta_{ij}|$. Moreover, the dispersion parameter offers a quantification of the St -separation relative to the overall inertia of the droplet pair. Based on this reasoning, we expect $\rho(\theta)$ to exhibit a more universal behavior compared to $\rho(\phi)$, which Fig. 3(b) confirms in the affirmative. The majority of data points collapse on an exponential curve, so that

$$\rho(\theta) = 0.77 * \exp(-27.8\theta) + 1.93 \exp(-4.07\theta)^{\frac{1}{2}} [1 + \tanh(\theta - 1)] \quad (11)$$

provides an excellent fit to the DNS data. To obtain this expression, we used the composite formulation from the Zhou model and performed a least-squares fit on the $Re_\lambda = 418$ DNS data. Because of the singular behavior in the limit of vanishing Stokes number, droplet pairs involving very small St appear as outliers. For clarity, data points with $\min(St_i, St_j) \leq 0.1, 0.2$, and 0.3 are shown using distinct symbols and colors. By the same reasoning, outliers are also expected at large Stokes numbers, since a uniform spatial distribution is not only recovered in the small- St limit, but also as $St \rightarrow \infty$. To confirm this hypothesis, we extend our data set to include droplet pairs with $St = 4$ and plot these separately in Fig. 3(b). In general, we conclude that our formulation improves the predictions for the bidisperse correlation coefficient. Generalization to varying Reynolds numbers is deferred to future work.

2. A novel parameterization for the bidisperse collision kernel

Above, we showed that although the Onishi model accurately predicts monodisperse clustering, it produces large errors in the bidisperse case, as evident from Fig. 4(c). This limitation arises from its reliance on the Zhou model, which fails to capture the rapid decorrelation of particle clusters as St_i and St_j diverge. Having improved the bidisperse clustering predictions by introducing $\rho(\theta)$ in Eq. (11), we now move on to present a compact parameterization for the bidisperse collision kernel as a function of the dispersion parameter. This is motivated by the observation that the kernel varies smoothly as the Stokes numbers separate, whereas both the RDF and RRV do not. Letting $\tau = St_i + St_j$ and $\delta = St_i - St_j$, we consider the first-order approximation $\Gamma(\tau, \delta) = \Gamma(\tau, 0) + E(\tau) \frac{\delta}{\tau} + \mathcal{O}(\delta^2)$. Here, the sign and magnitude of the polydisperse 'enhancement factor' $E(\tau)$ depend on the overall inertia τ , but not on the separation δ . As established earlier, the effect of polydispersity arises from the competition between increased relative velocities and reduced preferential concentration as St_i and St_j diverge. To quantify this balance, we seek a reference quantity that isolates the velocity enhancement from spatial correlations. On the basis of empirical observations, we find that the kernel Γ_{0i} —defined for interactions between tracer-like droplets ($St_0 \ll 1$) and inertial ones (St_i)—provides a suitable measure, since it primarily reflects the contribution from differential sampling. Hence, the net enhancement due to polydispersity is approximated by the difference $E(\tau) = \Gamma_{0i} - \Gamma_{ii}$.

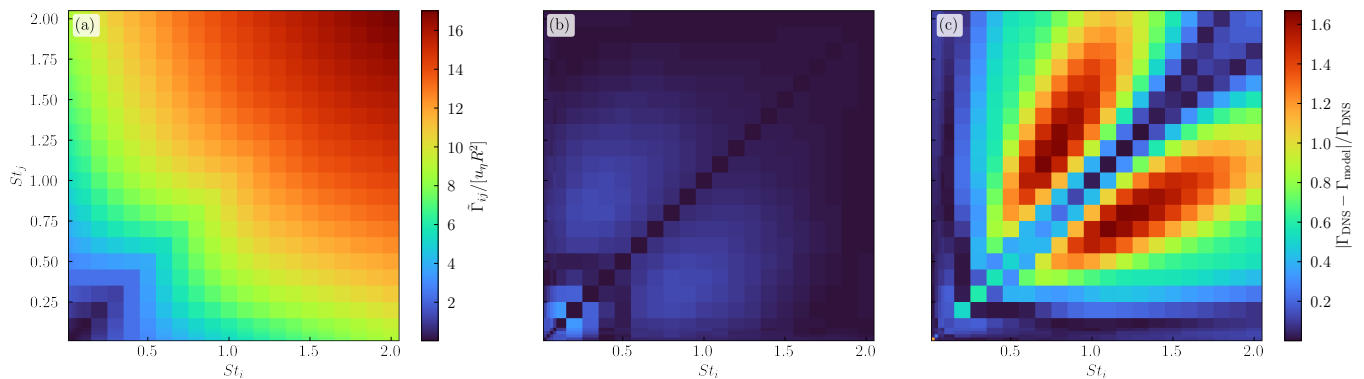


FIG. 4. (a) Bidisperse collision kernel matrix computed from Eq. (12) with Γ_{ii} and Γ_{0i} obtained from the DNS ($St_0 = 0.02$) and (b) its relative error with respect to the DNS data. (c) The relative error with respect to the DNS data obtained with the Onishi model. Panels (b) and (c) share the same color scale shown on the right.

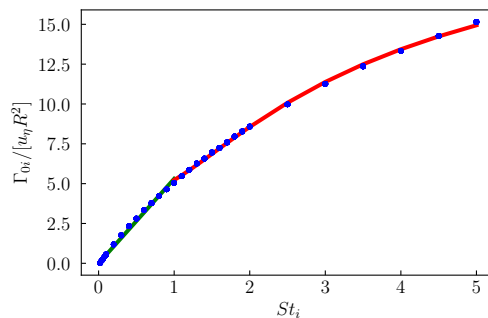


FIG. 5. Γ_{0i} obtained from the DNS with $St_0 = 0.02$ (blue dots). The green and red lines depict the empirical fits $\Gamma_{0i} = aSt_i$ with $a = 5.3$ and $\Gamma_{0i} = b_0 + b_1 \exp(-b_2/St_i)$ with $b_0 = 4.3$, $b_1 = 19.6$, $b_2 = 3.05$, respectively.

Following this approach, we find that the bidisperse collision kernel for a droplet pair (i, j) with $St_i \geq St_j$ can be effectively parameterized as

$$\tilde{\Gamma}_{ij} = \theta_{ij}\Gamma_{0i} + (1 - \theta_{ij})\Gamma_{ii}. \quad (12)$$

Here, Γ_{ii} is the monodisperse collision kernel and Γ_{0i} is the collision kernel between particles of St_i and very light, close-to-tracer particles (shown in Fig. 5 with $St_0 = 0.02$). The parameterization is given for $St_i \geq St_j$ so that $\theta_{ij} \geq 0$, but extension to arbitrary pairs follows trivially from symmetry. The heuristic behind expression (12) is the separation of the collision kernel into inertial effects (preferential concentration and the sling effect, represented by the monodisperse kernel) and differential sampling (represented by Γ_{0i}). Here, Γ_{ii} corresponds to the diagonal and Γ_{0i} to the bottom row (or first column) of Fig. 2(a). The resulting bidisperse kernel is a 'blend' of the two contributions, weighted by the dispersion parameter θ_{ij} . One easily verifies that as $St_j \rightarrow 0$, the correct asymptotic behavior $\tilde{\Gamma}_{ij} = \Gamma_{0i}$ is recovered. Similarly, for $i = j$, Eq. (12) simplifies to the monodisperse collision kernel.

Figure 4(a) displays the predictions of Eq. (12), allowing direct comparison to the DNS reference (Fig. 2(a)). The compact linear formulation captures the effect of differential sampling on the collision kernel with remarkable qualitative accuracy. It reproduces the enhancement due to polydispersity at small Stokes numbers, even when the mean Stokes number of the colliding pair is reduced. This behavior arises because initially, Γ_{0i} increases more rapidly with St_i through differential sampling than Γ_{ii} increases through inertial effects, leading to $\Gamma_{0i} > \Gamma_{ii}$ for small St_i and $\Gamma_{ii} > \Gamma_{0i}$ for $St_i \gtrsim 0.4$.

The relative error of our model with respect to the DNS data is shown in Fig. 4(b). The predictions generally agree with the DNS results to within 10%. Larger errors are seen primarily for small Stokes numbers around the diagonal, since the collision kernel is close to 0 in this region, thus amplifying the error signal. Unequivocally, the predictions of our parameterization match the DNS data much better compared to the Onishi model, whose relative error is shown in Fig. 4(c). The model predictions deviate from the DNS reference especially for bidisperse droplet pairs with $St \gtrsim 1$, where the overestimation of the bidisperse correlation coefficient following Eq. (8) is most pronounced.

TABLE I. Scaling factor α , mean Stokes number, corresponding increase in the local dissipation rate and initial number of droplets.

α	$\langle St \rangle$	$\varepsilon/\varepsilon_0$	$N_p(t=0)$
1	0.23	1	$5 \cdot 10^8$
1.33	0.4	3.13	$2.1 \cdot 10^8$
1.75	0.69	9.38	$9.3 \cdot 10^7$
2.1	1	19.45	$5.3 \cdot 10^7$

Recall that Γ_{0i} describes the collisions between droplets with $St_0 \ll 1$ (tracer-like) and St_i . In order for Eq. (12) to yield a complete model for the bidisperse collision kernel, an explicit expression for Γ_{0i} is required (whereas Γ_{ii} can be modelled with the Onishi model). In this situation, preferential concentration is negligible ($g_{i0}(R) \approx 1$ for sufficiently small St_0), and the collision dynamics are dominated by the RRV. James & Ray [6] derived analytical expressions for $\langle w_r \rangle$ under various limiting assumptions. They demonstrate that with $St_j \ll 1$, the RRV obeys the linear scaling $w_r \sim St_i$ if $St_i \lesssim 1$ and exponential scaling of the form $w_r \sim \exp(-1/St_i)$ for $St_i \gg 1$. Since $g(R) \approx 1$ in this regime, we can apply the scaling of the RVV to that of the collision kernel. In Fig. 5, we show the Γ_{0i} kernel obtained by approximating $St_0 = 0.02$ and apply the two scaling laws. It is evident that the kernel agrees well with the resulting fits.

C. Turbulent broadening of the droplet size distribution

We now move away from the ghost collision approach and turn to simulations with coalescing droplets. These simulations allow us to study the turbulent broadening of the droplet size distribution (DSD), without relying on the simplifying assumptions of stochastic collision-coalescence models, which are known to underestimate the rapid formation of 'lucky' droplets through successive correlated collisions [40]. As discussed in the Introduction, the inertia and settling of cloud droplets vary along their trajectories due to random fluctuations of the local turbulence intensity; hence, droplet growth in the bottleneck range depends strongly on the instantaneous local dissipation rate, ε . In order to study the effect of ε on droplet growth without performing additional simulations at larger Reynolds numbers, we exploit the fact that the Stokes number scales as $St \propto r^2 \varepsilon^{1/2}$. Thus, increasing the dissipation rate by a factor α^4 is equivalent to increasing the droplet size by α while keeping the flow field unchanged. This equivalence allows us to emulate fluctuations of the dissipation rate by scaling the initial DSD rather than performing computationally expensive DNS at higher Reynolds numbers.

We stress once more that all simulations are performed at fixed $Re_\lambda = 418$, well below the realistic values in atmospheric clouds ($\mathcal{O}(10^4)$). As noted in the Introduction, clustering shows a weak, yet non-negligible Re_λ -sensitivity, since extrapolation of the DNS to atmospheric conditions spans at least one order of magnitude. On the basis of the cited reports [22–24], we therefore expect our simulations to slightly overestimate the growth of droplets with $0.4 \lesssim St \lesssim 1$ and to underestimate it for $St \gtrsim 1$. At higher Re_λ , dissipation rate fluctuations become more intense yet more localized in space and time. While the aim of our study is to demonstrate accelerated droplet growth in highly dissipative parcels, by no means do we claim that our simulations reproduce the cloud-realistic intermittency of ε .

Droplet populations are initialized with radii following a Gaussian distribution, $r \sim \mathcal{N}(r_0, \sigma_r^2)$, with mean r_0 and standard deviation σ_r , as is expected to result from condensation. Both r_0 and σ_r are then scaled by α , so that a shift in the local energy dissipation rate by a factor of $\varepsilon/\varepsilon_0 = \alpha^4$ is emulated. For example, by setting $\alpha = 1.75$, we adjust the mean Stokes number from $\langle St \rangle = 0.23$ to $\langle St \rangle = 0.69$, corresponding to a 9.38-fold increase in the local energy dissipation rate, which is well within measurements in atmospheric clouds [17]. All simulated cases are tabulated in Table I. To keep the droplet volume fraction $\Phi_p \propto nr^3$ unchanged, the initial number of droplets, $N_p(t=0)$, is reduced as α grows. A cloud-realistic value of $\Phi_p = 8.5 \cdot 10^{-6}$ is kept constant throughout the simulation campaign.

The initial state of the base case ($\alpha = 1$) exhibits a mean Stokes number of $\langle St \rangle = 0.23$, mean radius $r_0 = 0.036\eta$ and standard deviation $\sigma_r = 0.00179\eta$. With an estimate of $\mathcal{O}(\eta) = 10^{-1}$ mm [1, 17] in atmospheric conditions, the base case is representative of droplets at the lower end of the bottleneck range. The time evolution of the DSD for the base case is shown in Fig. 6(a). The droplet size is given in terms of the Stokes number, and the curves show the probability density function (PDF) evaluated at equidistant bins. It is evident that the DSD broadens rapidly from its initial narrow Gaussian distribution (shown by the dashed blue curve), with large droplets appearing after short integration times. This indicates that turbulence by itself is effective in promoting droplet growth even for small, typical cloud droplets. The distributions develop long tails with 'bumpy' profiles, owing to the narrow initial distributions and the binary nature of coalescence events. Assuming a cloud-realistic Kolmogorov timescale

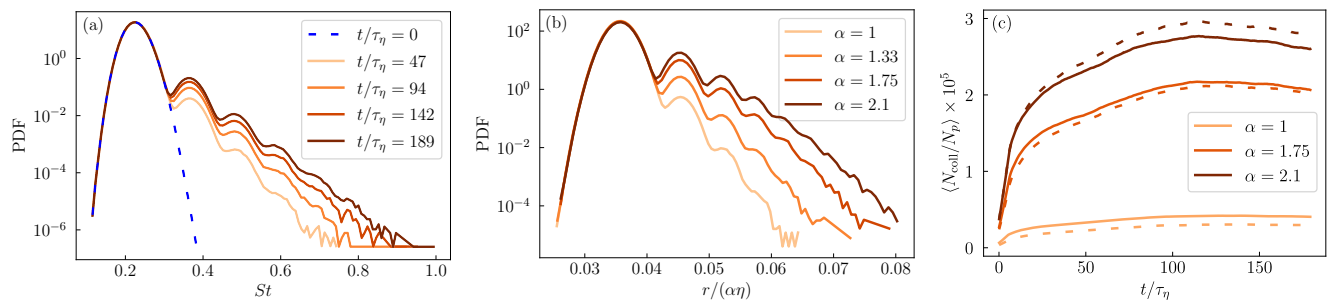


FIG. 6. Results for the DNS with coalescing droplets. (a) Evolution of the DSD given by the probability distribution function of the droplet Stokes number obtained from the base case ($\alpha = 1$). The initial distribution is shown by the dashed blue curve. (b) DSDs in terms of the scaled droplet radius after $t = 189\tau_p$ for different values of α . (c) Evolution of the time-averaged rate of collision-coalescence (solid lines) for different values of α , along with monodisperse reference simulations (dashed lines).

of $\mathcal{O}(\tau_\eta) = 10^{-2}$ s [1, 17], the DSD evolution shown in Fig. 6(a) unfolds over time intervals much shorter than the typical lifetime of a cumulus cloud prior to the onset of precipitation. The DSD continues to broaden, even without the introduction of new droplets. After $t = 189\tau_\eta$, the largest droplets reach $St \approx 1$, corresponding to a radius of $r = 2r_0$.

Figure 6(b) depicts DSDs for different values of α after an integration time of $t = 189\tau_p$. In reality, an increase in the local dissipation rate would increase the Stokes number of a cloud droplet by decreasing the local instantaneous τ_η . In our study, however, the flow field remains unchanged while the droplet phase is altered. To ensure a consistent comparison of the DSDs across different α , the evaluation time was fixed in units of τ_p rather than the flow timescale. The curves in Figure 6(b) represent the PDFs of the droplet radii scaled back by the factor α . This means that the horizontal axis depicts the radii of the droplets under the conditions of the base case, approximately spanning the bottleneck range (again, assuming $\mathcal{O}(\eta) = 10^{-1}$ mm). We observe that the droplet growth significantly accelerates with increasing α . The fraction of droplets that overcome the size gap clearly grows with α , indicating that the local turbulence intensity effectively promotes droplet growth. The largest variations appear between the cases with $\alpha = 1$, $\alpha = 1.33$, and $\alpha = 1.75$, corresponding to increases in the mean Stokes number from $\langle St \rangle = 0.23$ to 0.4 and 0.69, respectively. This range marks the regime of strongest enhancement, consistent with the observations from Section IV A.

Figure 6(c) shows the time-averaged fraction of droplets that undergo collision and coalescence as it evolves in time. All cases exhibit statistical stationarity after around $t = 100\tau_\eta$. The collision rate strongly increases with α : compared to the base case, the collisions occur around 5.3 and 7 times more frequently with $\alpha = 1.75$ and $\alpha = 2.1$, respectively. This data supports the theory that short-lived intense turbulent events may significantly accelerate droplet growth. In addition, Figure 6(c) displays the collision-coalescence rates for monodisperse reference simulations (dashed lines). The reference simulations are initialized with monodisperse droplet populations of radius $r = \alpha r_0$. In the base case, the collision rate is around 50% higher compared to the monodisperse suspension, demonstrating that polydispersity effectively enhances droplet growth. For the case with $\alpha = 1.75$, on the other hand, the polydisperse enhancement reduces to merely 5%. At $\alpha = 2.1$, the effect of polydispersity switches from collision-enhancing to attenuating, and the monodisperse collision rate is around 5% larger. Again, these findings are consistent with the results obtained in Section IV B. Depending on the local turbulence intensity, narrow DSDs in atmospheric clouds can therefore broaden more rapidly than wider ones.

V. DISCUSSION

We have studied polydisperse droplet collisions in homogeneous isotropic turbulence at $Re_\lambda = 418$ by means of direct numerical simulations (DNSs). The bidisperse collision kernel, relative radial velocity (RRV) and radial distribution function (RDF) at contact have been obtained for droplet pairs with Stokes numbers in the range $St \in [0.02, 2]$. This data is important for understanding how turbulence affects the growth of droplets in warm atmospheric clouds. The simulations were performed in the absence of gravity, to address specifically the cloud droplet bottleneck range, within which droplets cannot grow effectively by diffusion yet are not heavy enough to collide under gravitational settling.

Our findings establish that differential sampling is an effective mechanism by which differently-sized droplets collide under turbulence, even in the absence of gravity. This contrasts with the conventional view that primarily links polydispersity to collisions induced by gravitational settling and challenges cloud microphysics schemes to incorporate

these effects. Droplets with separate relaxation times cluster less, but have larger relative velocities, so that the influence of polydispersity is highly dependent on the Stokes number. At $St \lesssim 0.5$, polydispersity enhances collisions because the increased relative velocities from differential sampling compensate the reduction in clustering. Conversely, at larger Stokes numbers, preferential concentrations and the sling effect are the dominant collision mechanisms, and polydispersity attenuates collisions in this regime because it rapidly decorrelates the number density fields of differently-sized droplets. Thus, the role of polydispersity transitions from being a facilitator to a suppressor of collisions as particle inertia increases.

We have compared our DNS with the Onishi model [23] and found good agreement for the monodisperse collision kernel up to $St \approx 1.5$. In contrast, the Zhou model [8] was shown to introduce errors in the bidisperse RDF, because it underestimates the rapid decorrelation of the spatial distribution of droplets as the Stokes numbers separate. We attribute this to a Reynolds number dependence of the correlation between the number density fields of droplets with different Stokes numbers, since larger Reynolds numbers introduce increased separations of length scales that droplets of different relaxation times sample preferentially. Additional simulations at varying Re_λ should be conducted to clarify this effect. An improved version of the Zhou model for the bidisperse correlation coefficient has been proposed, which at fixed Re_λ was demonstrated to achieve better agreement with the DNS data.

We have introduced a new compact expression for the bidisperse collision kernel. This parameterization originates from the observation that, although the underlying bidisperse RRV and RDF display difficult-to-model variability with respect to St_i and St_j , the bidisperse collision kernel in itself varies smoothly with the Stokes number separation. By exploiting symmetries and identifying the dispersion parameter θ_{ij} as the relevant measure, our model results from a first-order approximation that reproduces the DNS reference with remarkable accuracy. Future work should test the parameterization for varying Reynolds numbers, extend it to include gravity, and establish (or refute) a theoretical foundation for its validity.

Simulations of coalescing droplets have shown that turbulence alone can bridge the cloud droplet size gap. Rapid broadening of the droplet size distribution (DSD) was observed even for typical cloud droplets with Stokes numbers around $St \approx 0.2$, providing a viable pathway for growth within the bottleneck range. We further examined DSD broadening under emulated fluctuations of the local dissipation rate and found that droplet growth is markedly accelerated in highly dissipative parcels. Depending on the droplet size and local turbulent intensity, initially narrow DSDs can broaden faster than wider ones, underscoring the complex, nontrivial link between the local flow conditions, the initial population and its evolution.

These results support the long-standing hypothesis that turbulent intermittency may play a central role in overcoming the bottleneck problem. Our evidence is limited, however, to fixed Reynolds numbers smaller than those in actual clouds. Numerical simulations are unlikely to reproduce turbulent flows that rival atmospheric conditions in the foreseeable future. Given these constraints, complementary approaches such as in-situ high-definition holographic imaging appear most promising to clarify this issue.

Looking ahead, we plan to incorporate our findings into the microphysics scheme of large-eddy simulations (LESs) of convective clouds. This will enable a more accurate representation of polydispersity, which appears to be under-represented in current models. In LESs, the intermittent distribution of the dissipation rate is supplied by the flow, and the dependence of the collision rate on ε enters through the Stokes number, which consequently varies along droplet trajectories. This framework will allow us to investigate the role of turbulence in a more realistic, large-scale atmospheric context to better quantify its impact on droplet growth and rain formation.

ACKNOWLEDGMENTS

This research was supported by funding from the Swiss National Science Foundation (grant 204621). Numerical simulations were carried out using the resources provided by the Euler cluster of ETH Zürich.

AUTHOR CONTRIBUTIONS STATEMENT

L.A.C. performed the simulations. All authors analyzed the results. D.W.M. lead the acquisition of funding. P.J. supervised the project. L.A.C. wrote the original manuscript. All authors reviewed the manuscript.

Appendix A: Onishi model for the monodisperse radial distribution function

The Onishi model [23] for the monodisperse radial distribution function is

$$g_{ii}(R) - 1 = \begin{cases} A_1 St^2 & (\equiv y_1) \quad (\text{for } St_i < St_a) \\ A_2 Re_\lambda St^{-2} & (\equiv y_2) \quad (\text{for } St_a \leq St_i) \end{cases}, \quad (\text{A1})$$

with $A_1 = 110$, $A_2 = 0.38$ and $St_a = ((A_2/A_1)Re_\lambda)^{1/4}$. The two formulations are connected in the composite expression

$$g_{ii} - 1 = H(St - St_a)y_1 z_a^\alpha + H(St_a - St)y_2(1 - z_a)^\alpha, \quad (\text{A2})$$

where $H(\cdot)$ denotes the Heaviside function and

$$z_a(St) = \frac{1}{2} \left(1 - \tanh \frac{\log_{10} St - \log_{10} St_a}{C_a} \right) \quad (\text{A3})$$

with $C_a = a_c Re_\lambda^{b_c}$, $\alpha = \log_2(a_\alpha Re_\lambda^{b_\alpha})$, $a_c = 0.046$, $b_c = 0.36$, $a_{c2} = 0.094$, $b_{c2} = 0.25$, $a_\alpha = 0.23$ and $b_\alpha = 0.5$.

Appendix B: Wang model for the radial relative velocity

The Wang model [30] for the radial relative velocity is

$$\langle w_r \rangle = \left[\frac{2}{\pi} (w_{\text{shear}}^2 + w_{\text{accel}}^2) \right]^{1/2}, \quad (\text{B1})$$

with

$$w_{\text{shear}}^2 = \frac{R^2 \varepsilon}{15\nu}, \quad (\text{B2a})$$

$$w_{\text{accel}}^2 = \frac{1}{3} C_w(\phi) f_{KK}, \quad (\text{B2b})$$

$$f_{KK} = \frac{\gamma u_{\text{rms}}^2}{\gamma - 1} \left\{ (\xi_i + \xi_j) - \frac{4\xi_i \xi_j}{(\xi_i + \xi_j)} \left[\frac{1 + \xi_i + \xi_j}{(1 + \xi_i)(1 + \xi_j)} \right]^{1/2} \right\} \times \left[\frac{1}{(1 + \xi_i)(1 + \xi_j)} - \frac{1}{(1 + \gamma\xi_i)(1 + \gamma\xi_j)} \right], \quad (\text{B2c})$$

where f_{KK} was adapted from Kruis & Kusters [41], $C_w(\phi) = 1 + 0.6 \exp[-(\phi - 1)^{3/2}]$ was provided later on by Zhou et al. [8], $\phi = \max(St_i/St_j, St_j/St_i)$, $\gamma = 0.183 u_{\text{rms}}^2 / (\varepsilon\nu)^{1/2}$ and $\xi_i = \tau_{p,i} / (0.4 u_{\text{rms}}^2 / \varepsilon)$.

Appendix C: Collision map

The map of collision kernels obtained from the DNS is provided in Table II.

-
- [1] W. W. Grabowski and L.-P. Wang, Growth of Cloud Droplets in a Turbulent Environment, *Annual Review of Fluid Mechanics* **45**, 293 (2013).
 - [2] M. R. Maxey, The gravitational settling of aerosol particles in homogeneous turbulence and random flow fields, *Journal of Fluid Mechanics* **174**, 441 (1987).
 - [3] K. D. Squires and J. K. Eaton, Preferential concentration of particles by turbulence, *Physics of Fluids A: Fluid Dynamics* **3**, 1169 (1991).
 - [4] M. Cencini, J. Bec, L. Biferale, G. Boffetta, A. Celani, A. S. Lanotte, S. Musacchio, and F. Toschi, Dynamics and statistics of heavy particles in turbulent flows, *Journal of Turbulence* **7**, N36 (2006).
 - [5] B. Ray and L. R. Collins, Preferential concentration and relative velocity statistics of inertial particles in Navier–Stokes turbulence with and without filtering, *Journal of Fluid Mechanics* **680**, 488 (2011).
 - [6] M. James and S. S. Ray, Enhanced droplet collision rates and impact velocities in turbulent flows: The effect of polydispersity and transient phases, *Scientific Reports* **7**, 12231 (2017).

TABLE II. Collision kernel $\Gamma_{ij}/[u_\eta R^2]$ map obtained from the DNS.

St_j	St_i												
	0.02	0.04	0.06	0.08	0.10	0.20	0.30	0.40	0.50	0.60	0.70	0.80	
0.02	0.01277												
0.04	0.16505	0.03156											
0.06	0.27601	0.18060	0.04540										
0.08	0.42849	0.32645	0.19559	0.05710									
0.10	0.55848	0.43573	0.38224	0.22440	0.08234								
0.20	1.18572	1.15355	1.08286	1.02224	0.97912	0.37916							
0.30	1.75848	1.76843	1.77923	1.77484	1.76012	1.53078	1.12224						
0.40	2.33210	2.33557	2.37930	2.35424	2.43812	2.49352	2.40884	2.32468					
0.50	2.80317	2.90411	2.94668	2.98532	3.08258	3.31190	3.47191	3.57487	3.83268				
0.60	3.34826	3.37947	3.50426	3.62061	3.67220	4.03588	4.35560	4.67199	4.92353	5.47079			
0.70	3.77795	3.89934	4.03519	4.12801	4.24232	4.68762	5.12753	5.53584	5.94911	6.32796	7.02727		
0.80	4.23107	4.29048	4.47630	4.63539	4.74826	5.28461	5.80139	6.27735	6.76131	7.24059	7.69620	8.47691	
0.90	4.64595	4.79775	4.95827	5.08948	5.23134	5.84230	6.39364	6.94093	7.45838	7.97397	8.47879	8.95773	
1.00	5.04391	5.23472	5.40776	5.49184	5.71050	6.37854	6.94472	7.50873	8.07235	8.60634	9.12294	9.62640	
1.10	5.47413	5.61282	5.78722	5.99485	6.14037	6.84488	7.47552	8.05002	8.60680	9.16491	9.68390	10.19766	
1.20	5.87031	6.07145	6.29976	6.41718	6.56181	7.30054	7.94147	8.55174	9.10734	9.65539	10.17576	10.68197	
1.30	6.26329	6.42922	6.65058	6.80364	6.96769	7.73206	8.38670	8.99183	9.55760	10.10592	10.62200	11.11586	
1.40	6.56997	6.78774	7.01080	7.25122	7.37456	8.13744	8.81393	9.42241	9.98184	10.52753	11.03023	11.53312	
1.50	6.95576	7.13769	7.35240	7.56837	7.73235	8.53061	9.21013	9.80487	10.36470	10.89951	11.41620	11.89506	
1.60	7.24463	7.51275	7.76437	7.93532	8.10387	8.89641	9.58548	10.18556	10.73761	11.27000	11.75116	12.24358	
1.70	7.58767	7.83312	8.11416	8.27969	8.43659	9.25581	9.93697	10.52769	11.08823	11.59651	12.08824	12.56969	
1.80	7.95646	8.15233	8.41134	8.59501	8.77807	9.58937	10.25929	10.85981	11.42777	11.92092	12.41594	12.86127	
1.90	8.27695	8.47734	8.71739	8.89287	9.10369	9.92090	10.59204	11.20353	11.73089	12.23876	12.71681	13.16148	
2.00	8.57909	8.80738	9.04030	9.24321	9.40503	10.23063	10.91301	11.50724	12.04071	12.54522	13.00085	13.45026	

St_j	St_i												
	0.90	1.00	1.10	1.20	1.30	1.40	1.50	1.60	1.70	1.80	1.90	2.00	
0.90	9.76041												
1.00	10.09796	10.90254											
1.10	10.67080	11.13321	11.89235										
1.20	11.15457	11.60663	12.04728	12.76147									
1.30	11.58628	12.03481	12.46798	12.86599	13.49508								
1.40	12.00200	12.42059	12.84020	13.22151	13.59128	14.16792							
1.50	12.35090	12.77632	13.17037	13.54058	13.88874	14.23512	14.75199						
1.60	12.67264	13.10950	13.50208	13.85476	14.20252	14.50091	14.81292	15.30091					
1.70	12.99965	13.40392	13.78696	14.13359	14.47433	14.77624	15.05530	15.32526	15.75626				
1.80	13.29551	13.69588	14.06014	14.41193	14.73226	15.02399	15.30795	15.55688	15.82958	16.22575			
1.90	13.58672	13.97629	14.32550	14.67578	14.98400	15.27341	15.54030	15.80063	16.03085	16.28500	16.62634		
2.00	13.84152	14.23137	14.58503	14.90659	15.22223	15.50815	15.76992	16.02545	16.24249	16.46829	16.69572	16.99660	

- [7] V. Nair, B. Devenish, and M. van Reeuwijk, Effect of Gravity on Particle Clustering and Collisions in Decaying Turbulence, *Flow, Turbulence and Combustion* **110**, 889 (2023).
- [8] Y. Zhou, A. S. Wexler, and L.-P. Wang, Modelling turbulent collision of bidisperse inertial particles, *Journal of Fluid Mechanics* **433**, 77 (2001).
- [9] G. Falkovich, A. Fouxon, and M. G. Stepanov, Acceleration of rain initiation by cloud turbulence, *Nature* **419**, 151 (2002).
- [10] M. Wilkinson and B. Mehligh, Caustics in turbulent aerosols, *Europhysics Letters (EPL)* **71**, 186 (2005).
- [11] J. Meibohm, L. Sundberg, B. Mehligh, and K. Gustavsson, Caustic formation in a non-Gaussian model for turbulent aerosols, *Physical Review Fluids* **9**, 024302 (2024).
- [12] L. A. Codispoti, D. W. Meyer, and P. Jenny, Dissecting inertial clustering and sling dynamics in high-Reynolds number particle-laden turbulence, *Physics of Fluids* **37**, 015161 (2025).
- [13] G. P. Bewley, E.-W. Saw, and E. Bodenschatz, Observation of the sling effect, *New Journal of Physics* **15**, 083051 (2013).
- [14] P. Deepu, S. Ravichandran, and R. Govindarajan, Caustics-induced coalescence of small droplets near a vortex, *Physical Review Fluids* **2**, 024305 (2017).
- [15] I. Fouxon, S. Lee, and C. Lee, Intermittency and collisions of fast sedimenting droplets in turbulence, *Physical Review Fluids* **7**, 124303 (2022).

- [16] S. Ravichandran and R. Govindarajan, Waltz of tiny droplets and the flow they live in, *Physical Review Fluids* **7**, 110512 (2022).
- [17] H. Siebert, R. A. Shaw, J. Ditas, T. Schmeissner, S. P. Malinowski, E. Bodenschatz, and H. Xu, High-resolution measurement of cloud microphysics and turbulence at a mountaintop station, *Atmospheric Measurement Techniques* **8**, 3219 (2015).
- [18] M. M. Feist, C. D. Westbrook, P. A. Clark, T. H. Stein, H. W. Lean, and A. J. Stirling, Statistics of convective cloud turbulence from a comprehensive turbulence retrieval method for radar observations, *Quarterly Journal of the Royal Meteorological Society* **145**, 727 (2019).
- [19] B. Thiede, M. L. Larsen, F. Nordsiek, O. Schlenczek, E. Bodenschatz, and G. Bagheri, *Highly Localised Droplet Clustering in Shallow Cumulus Clouds* (2025), [arXiv:2502.19272](https://arxiv.org/abs/2502.19272) [physics].
- [20] N. Allwayin, M. L. Larsen, S. Glienke, and R. A. Shaw, Locally narrow droplet size distributions are ubiquitous in stratocumulus clouds, *Science* **384**, 528 (2024).
- [21] R. Onishi and J. C. Vassilicos, Collision statistics of inertial particles in two-dimensional homogeneous isotropic turbulence with an inverse cascade, *Journal of Fluid Mechanics* **745**, 279 (2014).
- [22] R. Onishi, K. Matsuda, and K. Takahashi, Lagrangian Tracking Simulation of Droplet Growth in Turbulence—Turbulence Enhancement of Autoconversion Rate* [10.1175/JAS-D-14-0292.1](https://doi.org/10.1175/JAS-D-14-0292.1) (2015).
- [23] R. Onishi and A. Seifert, Reynolds-number dependence of turbulence enhancement on collision growth, *Atmospheric Chemistry and Physics* **16**, 12441 (2016).
- [24] P. J. Ireland, A. D. Bragg, and L. R. Collins, The effect of Reynolds number on inertial particle dynamics in isotropic turbulence. Part 1. Simulations without gravitational effects, *Journal of Fluid Mechanics* **796**, 617 (2016).
- [25] S. Sundaram and L. R. Collins, Collision statistics in an isotropic particle-laden turbulent suspension. Part 1. Direct numerical simulations, *Journal of Fluid Mechanics* **335**, 75 (1997).
- [26] L.-P. Wang, A. S. Wexler, and Y. Zhou, Statistical mechanical descriptions of turbulent coagulation, *Physics of Fluids* **10**, 2647 (1998).
- [27] F. Hoffmann, Y. Noh, and S. Raasch, The Route to Raindrop Formation in a Shallow Cumulus Cloud Simulated by a Lagrangian Cloud Model, *Journal of the Atmospheric Sciences* **74**, 2125 (2017).
- [28] K. K. Chandrakar, H. Morrison, W. W. Grabowski, and R. P. Lawson, Are turbulence effects on droplet collision-coalescence a key to understanding observed rain formation in clouds?, *Proceedings of the National Academy of Sciences* **121**, e2319664121 (2024).
- [29] O. Ayala, B. Rosa, and L.-P. Wang, Effects of turbulence on the geometric collision rate of sedimenting droplets. Part 2. Theory and parameterization, *New Journal of Physics* **10**, 075016 (2008).
- [30] L.-P. Wang, A. S. Wexler, and Y. Zhou, Statistical mechanical description and modelling of turbulent collision of inertial particles, *Journal of Fluid Mechanics* **415**, 117 (2000).
- [31] Y. Li, E. Perlman, M. Wan, Y. Yang, C. Meneveau, R. Burns, S. Chen, A. Szalay, and G. Eyink, A public turbulence database cluster and applications to study Lagrangian evolution of velocity increments in turbulence, *Journal of Turbulence* **9**, N31 (2008).
- [32] P. Jenny, M. Torrilhon, and S. Heinz, A solution algorithm for the fluid dynamic equations based on a stochastic model for molecular motion, *Journal of Computational Physics* **229**, 1077 (2010).
- [33] Message Passing Interface Forum, *MPI: A Message-Passing Interface Standard Version 4.0* (2021).
- [34] K. Gustavsson and B. Mehlig, Statistical models for spatial patterns of heavy particles in turbulence, *Advances in Physics* **65**, 1 (2016).
- [35] M. Vořkuhle, A. Pumir, E. Lévêque, and M. Wilkinson, Prevalence of the sling effect for enhancing collision rates in turbulent suspensions, *Journal of Fluid Mechanics* **749**, 841 (2014).
- [36] M. Wilkinson, B. Mehlig, and V. Bezuglyy, Caustic Activation of Rain Showers, *Physical Review Letters* **97**, 048501 (2006).
- [37] L. Pan and P. Padoan, Relative velocity of inertial particles in turbulent flows, *Journal of Fluid Mechanics* **661**, 73 (2010).
- [38] J. Abrahamson, Collision rates of small particles in a vigorously turbulent fluid, *Chemical Engineering Science* **30**, 1371 (1975).
- [39] S. Goto and J. C. Vassilicos, Self-similar clustering of inertial particles and zero-acceleration points in fully developed two-dimensional turbulence, *Physics of Fluids* **18**, 115103 (2006).
- [40] J. Bec, S. S. Ray, E. W. Saw, and H. Homann, Abrupt growth of large aggregates by correlated coalescences in turbulent flow, *Physical Review E* **93**, 031102 (2016).
- [41] F. E. Kruis and K. A. Kusters, The Collision Rate of Particles in Turbulent Flow, *Chemical Engineering Communications* **158**, 201 (1997).